RSC Advances

ROYAL SOCIETY OF CHEMISTRY

PAPER

View Article Online
View Journal | View Issue

Check for updates

Cite this: *RSC Adv.*, 2025, **15**, 11343

Mechanistic insights from simulations of drug–drug conjugate nanoclusters for co-delivery across cancer cell membranes†

Cherdpong Choodet, Unnop Srikulwong, Pakawat Toomjeen, Adulvit Chuaephon, Witthawat Phanchai and Theerapong Puangmali *

Received 20th January 2025
Accepted 4th April 2025

DOI: 10.1039/d5ra00480b

rsc.li/rsc-advances

Amphiphilic drug–drug conjugates (ADDCs) such as gemcitabine–camptothecin (**GEM–CPT**) and doxorubicin–10-hydroxycamptothecin (**DOX–HCPT**) nanoclusters offer innovative solutions to overcome the limitations of conventional cancer therapies, including poor solubility and nonspecific targeting. Using molecular dynamics (MD) simulations, we explored the mechanisms by which these nanoclusters interact with and penetrate cancer and normal cell membranes. **GEM–CPT** exhibited enhanced membrane penetration in cancer cells through combined hydrophilic and hydrophobic interactions, along with its ability to extract cholesterol and induce membrane remodelling. In contrast, **DOX–HCPT** maintained structural integrity through stable π–π stacking interactions, showing selective binding to membrane head groups (HG) with minimal cholesterol interaction, particularly in normal membranes. The **GEM–CPT** nanocluster disrupted the cancer membrane by inducing asymmetric lipid distribution and facilitating water infiltration, whereas the hydrophobic **DOX–HCPT** repelled water, maintaining membrane stability. The size of the nanocluster further influenced the behaviour; larger clusters drove steric assembly and lipid reorganisation, while smaller clusters achieved deeper penetration at the cost of structural integrity. The contrasting behaviours of **GEM–CPT** and **DOX–HCPT** highlight the critical roles of size, charge, and amphiphilicity in membrane transport mechanisms. These findings provide valuable insights into the design of efficient and selective nanomedicines, paving the way for optimised drug delivery systems with reduced off-target effects.

1 Introduction

The high incidence and mortality rates associated with cancer have fueled the continuous innovation of new anticancer treatment methods. Despite progress in this field, the significant side effects commonly linked to conventional therapies often undermine patient results, affecting both survival rates and life quality.[1] To alleviate these negative effects, combination chemotherapy, which uses multiple chemical agents to concurrently attack malignant tumours, has become a promising strategy.[2] Although combination therapies offer substantial benefits over single-drug options, their clinical effectiveness remains limited when administered *via* traditional dosage methods due to still-incomplete data on their results.[3] To overcome these challenges, amphiphilic drug conjugates (ADCs) have been developed as innovative co-delivery systems that tackle key hurdles in cancer treatment, such as multidrug resistance, inadequate bioavailability, and swift systemic elimination.[4,5] These advanced ADC platforms comprise various subcategories, including polymer–drug conjugates (PDCs), phospholipid–mimetic prodrugs, peptide–drug conjugates (PepDCs), pure nanodrugs (PNDs), Janus drug–drug conjugates (JDDCs), and amphiphilic drug–drug conjugates (ADDCs).[6] ADDCs represent a novel approach in cancer therapy, enhancing the effectiveness of combination chemotherapy due to their amphiphilic characteristics.[7] After biodegradation in tissues or cells, these conjugates release free anticancer agents that together target affected regions, which enhances cellular drug absorption. This technique has been advanced by binding hydrophilic and hydrophobic anticancer drugs to synergistically work. Through the integration of drugs with various physicochemical characteristics, ADDCs address significant issues such as low solubility, lack of target specificity, and poor pharmacokinetics.[8] These features promote efficient drug delivery and lead to better therapeutic results.

An illustrative case in this drug delivery model is the gemcitabine–camptothecin (**GEM–CPT**) conjugate, which has recently gained attention as a promising candidate in advanced drug delivery conjugates. Gemcitabine (**GEM**), a nucleoside analogue, inhibits DNA synthesis and is commonly used in the treatment of cancers such as the pancreas, breast, and lung.

Department of Physics, Faculty of Science, Khon Kaen University, Khon Kaen 40002, Thailand. E-mail: theerapong@kku.ac.th

† Electronic supplementary information (ESI) available. See DOI: https://doi.org/10.1039/d5ra00480b

Camptothecin (**CPT**), known for its strong inhibition of topoisomerase I, disrupts DNA replication and is especially effective against solid tumours. The amphiphilic properties of **GEM–CPT** conjugates facilitate their self-assembly into nanoparticles, improving the solubility and bioavailability. This attribute allows for the simultaneous release of drugs, achieving synergistic anticancer outcomes while reducing systemic toxicity. Due to their pharmacokinetic and pharmacodynamic benefits, **GEM–CPT** conjugates represent a highly effective and targeted drug delivery system, potentially overcoming the drawbacks of standard combination chemotherapies. Quantitative calculation of the combination index suggested that **GEM–CPT** exhibited a significant synergistic anticancer effect at elevated drug concentrations. According to research by Meili Hou *et al.*,[9] **GEM–CPT** efficiently circumvented tumour cell multidrug resistance.

In addition to the ADDCs, the PND model has been introduced as a novel approach to more efficient and less toxic drug delivery. The PND strategy eliminates the need for supplementary carriers or excipients by utilizing drug–drug conjugates that deliver to target cells *via* the formation of nanoparticles or nanoclusters entirely made up of active pharmaceutical ingredients.[10] PNDs represent a novel carrier-free drug delivery approach that incorporates multiple active drugs, enhancing anticancer effects.[10–13] The high hydrophobicity of chemotherapeutic agents poses a significant obstacle in the design and clinical application of nanomedicines.[14] Though various solubilizing agents and specific chemical modifications have somewhat reduced solubility issues, the dependency on additional agents such as surfactants remains an barrier to the clinical efficacy and translational prospects of these drugs. Better clinical outcomes are likely achieved by avoiding such methods of fabrication. An effective alternative is to employ the active pharmaceutical ingredients themselves as surfactants.

Doxorubicin (**DOX**), characterised by its hydrophobic anthracycline rings and abundant hydroxyl structure, exhibits surfactant-like properties, suggesting its role as a stabiliser for drug nanosizing.[15,16] As an active pharmaceutical ingredient, **DOX** avoids limitations associated with inactive ingredients, enabling dual-drug combination therapy in PND. Liang *et al.*[17] reported the development of a carrier-free PND combining 10-hydroxycamptothecin (**HCPT**) and **DOX**, referred to as doxorubicin–10-hydroxycamptothecin (**DOX–HCPT**), utilising a straightforward and environmentally friendly technique. The surfactant-like characteristics of **DOX** eliminated the need for additives, increasing both the solubility in water and the stability. Although **DOX**-based PNDs and **GEM–CPT** ADDCs hold considerable promise for enhanced drug delivery, the critical factor of their interaction with cellular membranes, which influences drug uptake and effectiveness, remains essential, particularly due to the structural and compositional variances between normal and cancerous cell membranes.

Cell membranes are vital for the absorption of drugs into cells, managing how therapeutic agents access healthy and cancerous cells. These membranes consist of a lipid bilayer with proteins embedded within, which function as selective barriers that regulate molecular entry and exit.[18] Typically, healthy cell membranes maintain a well-balanced lipid composition, asymmetric arrangement, and selective permeability, all of which are crucial to maintaining cellular stability. Conversely, altered lipid compositions and symmetrical distribution are common traits of various diseases, including cancer.[19] Cancer cells, known for their uncontrolled growth, demand increased biomolecule supplies, such as fatty acids and lipids.[20] To facilitate their rapid expansion, tumour cells enhance fatty acid biosynthesis to produce the necessary components for new membrane formation.[21–23] The profiles of lipids and phospholipids are notably altered in cancers, such as breast[24,25] and colorectal cancers, as well as chemoresistant tumours.[26] Notably, hepatocellular carcinoma cells display a quadrupled sphingomyelin profile and increased levels of unsaturated fatty acids compared to normal cells.

The distribution of the lipid profile within the plasma membrane, sustained by the actions of flippases and floppases, is vital for its function.[27,28] The outer leaflet is predominantly composed of phosphatidylcholine (PC) and sphingomyelin (SM), while the inner leaflet primarily comprises phosphatidylserine (PS) and phosphatidylethanolamine (PE). Understanding these membrane properties and uptake mechanisms is crucial for advancing drug design and enhancing therapeutic outcomes, as the membrane penetration ability of a drug is a key factor in its efficacy. In recent years, simulations of cancerous and normal cell membranes have become a popular approach to study how drugs enter cells. These investigations offer critical insights, elucidating how structural and compositional variations between these cell types impact drug uptake.[29,30]

To understand the intricate interactions between drugs and cell membranes, we employed atomistic molecular dynamics (MD) simulations. This research aimed to explore the molecular processes by which amphiphilic drug conjugates interact with and integrate into cell membranes using MD simulations. The study concentrated on two model drugs: ADDCs (**GEM–CPT**) and PNDs (**DOX–HCPT**). The study assessed the process by which these drugs form nanoclusters (Fig. 1(a) and (b)) and explored their interactions with both cancerous and healthy cell membranes (Fig. 1(c)). In addition, the study analysed drug transport mechanisms across membranes, offering insights into therapeutic effectiveness and targeted delivery.

2 Methods

2.1 Molecular dynamics simulation

2.1.1 Simulation details. All-atom molecular dynamics simulations were executed using GROMACS version 2020,[31] with the generalized AMBER force field (GAFF).[32,33] The AMBER force fields are known and well studied, offering high precision in depicting interactions within biomolecular systems,[34–36] including pharmaceuticals.[37] Various studies have shown that AMBER force fields are suitable for simulating polymeric nanoparticles, producing results that are consistent with experimental data.[38,39] All simulations were performed with an ensemble NPT at a maintained pressure of 1 bar and a temperature of 300 K, using Parrinello–Rahman for pressure coupling

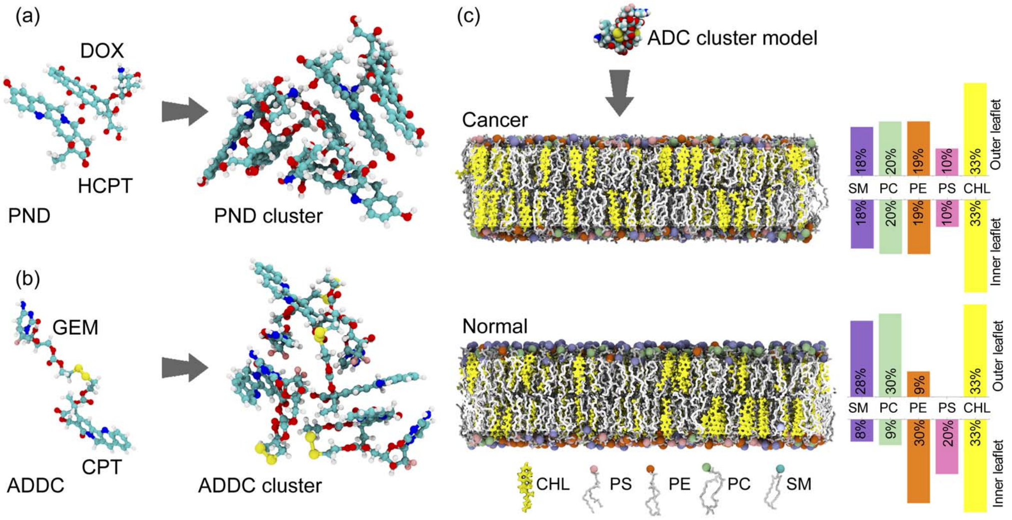

Fig. 1 (a) and (b) illustrate **DOX–HCPT** and **GEM–CPT** drug conjugates forming PND and ADDC nanoclusters, respectively. (c) Shows ADC nanoclusters interacting with both cancerous and normal membranes. Lipid components are colour-coded: sphingomyelin (SM) in purple, DOPE in orange, DOPS in pink, DOPC in green, and cholesterol (CHL) in yellow, with lipid head groups depicted as spheres. Histograms on the right reveal the normalized abundance of lipid species in the monolayers of the membranes.

and V-rescale for temperature control. The particle mesh Ewald (PME) method was employed to calculate long-range electrostatic interactions. This was succeeded by NPT equilibration for 5 ns at a constant temperature (300 K) and pressure (1 bar). Berendsen's thermostat with a coupling time of 1 ps and a barostat with a coupling time of 0.5 ps were applied to stabilise temperature and pressure throughout the simulations. The solvent accessible surface area (SASA) was calculated to examine the exposure of molecular surfaces to solvent environments in the simulations, using the GROMACS gmx SASA utility.[40,41] Observing SASA changes in simulations provides information on molecular interactions and behaviour, thus improving comprehension of drug delivery across different membrane types. The TIP3P model[42] was used to simulate water. Visualisation of all simulation results was performed using VMD (Visual Molecular Dynamics).[43]

2.1.2 Drug model. Two types of drug nanoclusters were developed: **GEM–CPT** ADDCs and **DOX–HCPT** PNDs nanoclusters. **GEM–CPT** ADDC consisted of gemcitabine and camptothecin linked through a disulfide bond, while **DOX** and **HCPT** were linked through self-assembly interactions in the absence of chemical bonds. To derive optimal configurations for each drug model, the Gaussian 09 software package was used with the HF/6-31G* basis set for C, H, O, N, F, and S atoms. ANTECHAMBER[44] was used to derive the partial charges of these molecules. For the development and structural refinement of drug nanoclusters, MD simulations were performed using the GROMACS 2020 package with the AMBER force field. Energy minimization, equilibration, and production MD simulations were conducted to assess the self-assembly mechanisms and stability of the nanoclusters in an explicit solvent environment. Specifically, the **GEM–CPT** and **DOX–HCPT** prodrug models were analysed for their ability to self-assemble into nanoaggregates in the absence of additional carrier materials, thereby forming an intrinsic drug delivery system. The nanoclusters of the drug–drug conjugate were formed through the self-assembly of drug molecules in the solvent. Initially, the ADDC and PND molecules were randomly dispersed in water within the simulation box of $10 \times 10 \times 10$ nm^3. They spontaneously aggregated into a nanocluster after 5 ns equilibration under NVT and NPT ensemble, respectively. From this ensemble, the most stable nanocluster configuration was selected based on structural integrity and minimised potential energy for subsequent studies on membrane interaction and internalisation.

2.1.3 Membrane model. The CHARMM-GUI membrane builder was used to create models for both cancer and normal membranes.[45–47] To optimise the membrane configuration, we began with energy minimisation to eliminate unfavourable interactions and stabilise the system. Then, a series of seven 5 ns equilibrium simulations were performed to assure system stability and the appropriate structural relaxation before proceeding with further analysis. The GAFF force field was used for drug molecules, whereas the AMBER Lipid14 force field was used for the membranes. The membrane system in this study was modelled with periodic boundary conditions (PBC) in all three dimensions to ensure a continuous and artefact-free representation of the lipid bilayer. This setup effectively eliminates artificial edges and maintains the integrity of the system by allowing molecules that exit one side of the simulation box to re-enter from the opposite side. The model referred to as the normal membrane was designed based on the asymmetry typical of mammalian plasma membranes, with the outer monolayer rich in SM and 1,2-dioleoyl-*sn*-glycero-3-phosphocholine (DOPC), and the inner monolayer containing a higher concentration of 1,2-dioleoyl-*sn*-glycero-3-phosphoethanolamine (DOPE) and 1,2-dioleoyl-*sn*-glycero-3-phospho-L-serine (DOPS).[29] To construct the cancer membrane, an increased proportion of DOPS and DOPE was incorporated into the extracellular leaflet. Cholesterol (CHL) was evenly distributed in both membrane models. The compositions of the normal and cancer membranes were aligned with existing experimental data.[48–50] The normal membrane was modelled on the lipid profiles that are well documented for mammalian membranes.[48] In the cancer membrane, the distribution of lipids was symmetrised to emphasise elevated levels of PS/PE in the extracellular leaflet. Detailed information regarding the lipid composition of the normal and cancer membrane monolayers can be found in Tables S1 and S2 within the ESI.†

2.1.4 Simulation setup. ADCs nanoclusters were positioned 2.5 nm above the upper leaflet of the membrane. The size of the simulation box is $9 \times 9 \times 12$ nm^3. In our MD simulations, periodic boundary conditions were applied in all three spatial dimensions. Following their placement, NaCl counterions were introduced into the simulation environment to achieve a salt concentration of 0.15 M at physiological levels. To explore how drug conjugate nanoclusters are internalised, pull simulations were executed that lasted up to approximately 6 nm along the z axis, which is perpendicular to the membrane plane. This was achieved by exerting a constant force of 1000 kJ mol nm^{-1} on the centre of mass (COM) with a pull rate of 0.0005 nm ps^{-1} of the ADC nanoclusters to facilitate their passage through the membrane. No transmembrane voltage or concentration gradient was applied across the bilayer. Instead, the translocation of the nanocluster was driven by a controlled pulling force using the umbrella sampling technique in the z-direction. This setup, with a force constant of 1000 kJ mol^{-1} nm^{-2} and a slow pull rate, allowed for accurate sampling while maintaining near-equilibrium dynamics. A comparable pull rate has been used to study the interactions between molecules or nanomaterials (such as polyethylene,[51] peptide,[52] and gold nanoparticle[53]) and cell membranes, showing that the process progresses progressively. This minimises non-physical distortions, thereby enabling the system to respond more naturally to the applied force. This method was used successfully to investigate the cellular uptake of gold nanoparticles in mammalian cells and can replicate the internalisation mechanisms seen in the experiment.[54]

2.2 Analysis

The Molecular Mechanics Poisson–Boltzmann Surface Area (MMPB-SA) tool integrated with GROMACS was utilized to calculate the free binding energy between the drug and the membrane.[55,56] The technique was originally developed to examine the binding interactions between proteins and ligands.[57] Later it has been widely used for various biomolecules.[56] Numerous studies have effectively applied this methodology to investigate the interactions among biomolecules, such as photosensitizers,[58] peptides,[59,60] with cell membranes. This calculation was carried out using gmx mmpbsa.[57] The binding free energy (G_{binding}) when the drug associates with the membrane in a solvent is determined by the following equation:[61]

$$\Delta G_{\text{binding}} = G_{\text{complex}} - (G_{\text{membrane}} + G_{\text{drug}}) \tag{1}$$

where G_{complex} indicates the total energy of the drug–membrane complex and G_{membrane} and G_{drug} denote the total energies of the membrane and drug separately in the solvent environment. Each free energy component is expressed as G_x (x refers to drug, membrane, or drug–membrane complex):

$$G_x = V^{\text{bonded}} + V^{\text{VdW}} + V^{\text{elec}} + G^{\text{polar}} + G^{\text{nonpolar}} - TS \tag{2}$$

with V^{bonded} accounting for energies due to bond stretching, angle bending, torsional angles, and improper dihedrals. Meanwhile, V^{VdW} and V^{elec} reflect van der Waals and electrostatic non-bonded interactions, respectively. The components G^{polar} and G^{nonpolar} represent the solvation free energies derived from an implicit continuum solvation model. Here, T and S are the system temperature and the vacuum entropy of the solute, respectively. The TS elements in eqn (2) illustrate the variation in conformational entropy when the drug binds to the membrane. Given that the conformation changes of the drug and the membrane in the bound and unbound states are negligible, the energies of V^{bonded} and the nonbonded intramolecular interaction cancel out in Eq. (2).[62] Hence,

$$\Delta G_{\text{binding}} = V^{\text{VdW}}_{\text{complex}} + V^{\text{elec}}_{\text{complex}} + \Delta G^{\text{polar}} + \Delta G^{\text{nonpolar}} \tag{3}$$

$$\Delta G^{\text{polar}} = G^{\text{polar}}_{\text{complex}} - (G^{\text{polar}}_{\text{drug}} + G^{\text{polar}}_{\text{membrane}}) \tag{4}$$

$$\Delta G^{\text{nonpolar}} = G^{\text{nonpolar}}_{\text{complex}} - (G^{\text{nonpolar}}_{\text{drug}} + G^{\text{nonpolar}}_{\text{membrane}}). \tag{5}$$

Here, G^{polar} and G^{nonpolar} are the electrostatic and non-electrostatic parts of the solvation free energy. The analysis of the variations in binding energy during the simulations offers insights into molecular interactions, conformational dynamics, and molecular behaviour in their environments, advancing our understanding of the complicated interactions between drug–drug conjugate nanoclusters and the cell membrane.

3 Results and discussion

To gain a comprehensive understanding of the cellular drug uptake mechanisms, we began by studying the structure of nanoclusters formed through the self-assembly of drug–drug conjugates. We then analysed the interactions between these drug nanoclusters and the cell membrane to assess how nanocluster size and configuration affect drug penetration. Lastly, we examined how co-delivery affects membrane deformation.

3.1 Structure of drug–drug conjugate nanocluster

The electrostatic distribution across the drug surface is crucial for identifying the position and intensity of both hydrophobic and hydrophilic areas, thereby aiding in the self-organization of drug molecules. **DOX** and **GEM** are abundant in functional groups that contain oxygen, such as ketones and hydroxyl groups. In contrast, **CPT** and **HCPT** have fewer oxygen-rich groups but consist of several bonded aromatic rings, as shown in their chemical structures and electrostatic potential (ESP) maps in Fig. 2. The red and blue areas on the ESP maps indicate significant polar zones, which indicate hydrophilic properties. Importantly, the joined aromatic rings present in **DOX** and **HCPT** facilitate robust π–π stacking interactions. **GEM–CPT** conjugates are classified as hydrophilic drug models exhibiting higher SASA, while **DOX** and **HCPT** serve as hydrophobic models with reduced SASA, as shown in Fig. S1.† Negative charges on the ESP surfaces correspond with electronegative atoms such as oxygen and nitrogen, while positive charges cluster on less electronegative atoms.

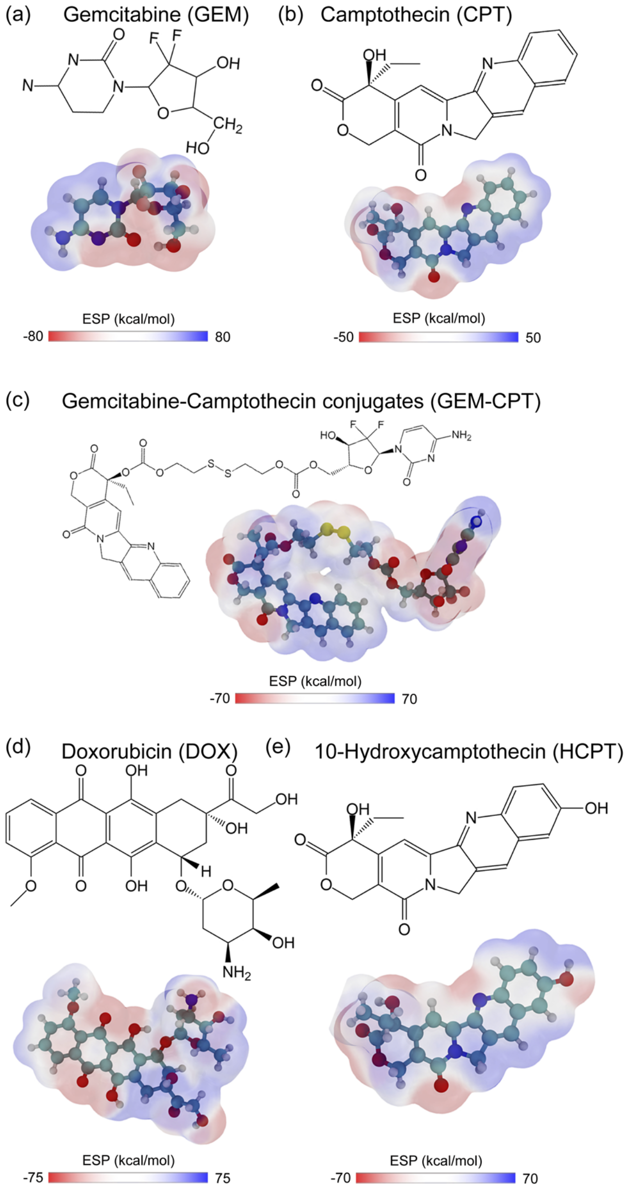

Fig. 2 Chemical structures and electrostatic potential (ESP) visualizations of pharmaceutical models. (a and b) Molecular structures of gemcitabine (**GEM**) and camptothecin (**CPT**) with corresponding ESP maps, highlighting regions of positive (blue) and negative (red) electrostatic potential. (c) Formation of **GEM–CPT** amphiphilic drug–drug conjugates (ADDCs), illustrating the integration of **GEM** and **CPT** *via* a disulfide linkage. (d and e) Molecular configurations of doxorubicin (**DOX**) and hydroxycamptothecin (**HCPT**) and the distribution of their electrostatic charge.

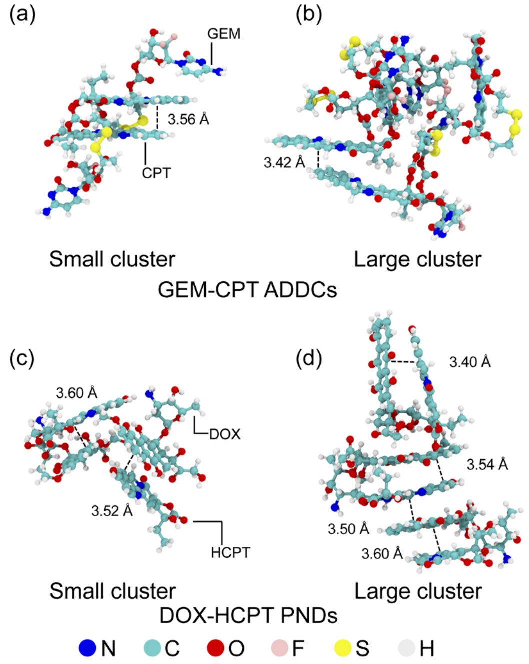

Fig. 3 Molecular configurations and π–π interactions in small and large aggregates of **GEM–CPT** and **DOX–HCPT**. The figure illustrates the aggregation structures of **GEM–CPT** (a and b) and **DOX–HCPT** (c and d), highlighting the π–π stacking interactions that stabilize these molecular assemblies. Distinct configurations for both small and large aggregates are depicted, emphasizing the role of π–π interactions in the self-assembly process.

The self-assembly of drug–drug conjugate nanoclusters in a solvent highlights the dynamic behaviour of drug molecules in an aqueous environment. Initially, amphiphilic drug–drug conjugates and pure nanodrugs were randomly distributed within the simulation box (Fig. S2 and S3†), but over time they self-organised into stable nanoclusters driven by thermodynamic forces. Fig. 3 compares the size-dependent structural effects of these nanoclusters. In smaller **GEM–CPT** ADDC nanoclusters, **CPT** molecules exhibit well-defined π–π stacking interactions with an interplanar distance of 3.56 Å, stabilised by aromatic interactions, while **GEM** adjusts its conformation to enhance non-covalent interactions with **CPT** rings (Fig. 3(a)). However, larger **GEM–CPT** nanoclusters show reduced stacking π–π among **CPT** molecules due to steric hindrance, with **GEM** primarily contributing to the bulk structure due to its disulfide tether, limiting its role in π–π interactions (Fig. 3(b)). In contrast, **DOX–HCPT** PNDs maintain consistent and highly ordered π–π stacking patterns in both small and large nanoclusters, as shown in Fig. 3(c) and (d), reflecting the structural advantage of their design. These findings underscore the crucial influence of steric effects and molecular architecture on nanocluster assembly and stability.

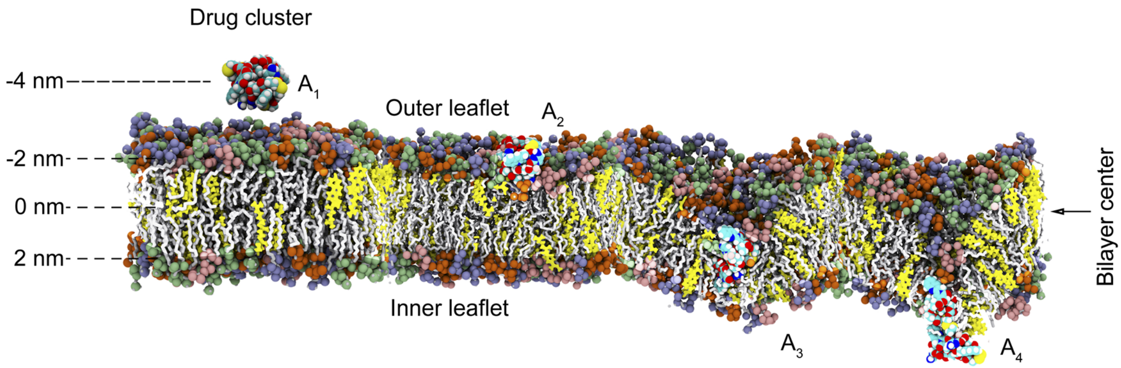

Fig. 4 Pathway of drug nanocluster penetration through the cell membrane. The 4 nm thick membrane comprises the outer leaflet, bilayer centre, and inner leaflet. The nanocluster transitions from floating near the surface (A_1) to interacting with the outer layer (A_2), embedding in the hydrophobic core (A_3), and penetrating the inner layer (A_4), entering the cell.

3.2 Influence of nanocluster size in cellular uptake

The process of cellular drug uptake is affected by the interaction between drug nanoclusters and the cell membrane, primarily influenced by the strength of the binding energy. To study these interactions, MD simulations were performed on **GEM–CPT** and **DOX–HCPT** nanoclusters of varying sizes, which react with normal and cancer cell membranes in an aqueous setting, as shown in Fig. 4. The large and small nanoclusters of both **GEM–CPT** ADDCs and **DOX–HCPT** PNDs, hereafter referred to as the large and small drug nanoclusters, were observed in this aqueous setting. The binding energy was examined at three critical sites: the outer leaflet, the centre of the bilayer, and the inner leaflet. Initially, the drug nanocluster contacts the outer leaflet (A_1) and begins to internalize into the membrane (A_2). As it advances to the bilayer centre (A_3), it interacts robustly with the hydrophobic core created by the lipid tails, showing considerable binding energy due to favourable hydrophobic interactions. Finally, the nanocluster penetrates the inner leaflet (A_4), moving further into the cell. The distance for each interaction phase was maintained at 2 nm, with the membrane initially set at a distance of zero relative to the centre of the simulation. In the analysis of binding energy, distances situated above the membrane's centre were designated as negative, while those located below were assigned positive values. These positional arrangements facilitated the evaluation of the binding energy relative to the distance throughout this study.

Experimental findings indicate that drug–drug conjugates have an average size of approximately 50 nm.[9,63] However, molecular simulations reduce this size to 1.5–4 nm to optimise computational efficiency.[6,9,63–67] Despite this reduction, simulations provide valuable insights into drug behaviour and development, as evidenced by studies on carrier-free self-assembled nanorods, even at reduced doses.[68] Fig. 5(a) and (b) highlights the critical role of nanocluster size in membrane permeability and cellular uptake. For larger **GEM–CPT** ADDC nanoclusters, the binding energy increases sharply as the cluster approaches −3.1 nm from the membrane centre, peaking at high positive values before declining after crossing this point. The minimum binding energy occurs at 2.7 nm for cancer membranes and 0.8 nm for normal membranes, followed by fluctuations as the nanocluster exits the membrane. MD simulations also reveal the extraction of cholesterol from the membrane, which adheres to the nanocluster and induces temporary deformation with slight curvature (Fig. 5(c) and (d)). This process, driven by hydrophobic interactions and steric effects, underscores the importance of sterically induced self-assembly. In normal membranes, higher concentrations of phosphatidylethanolamine (PE) in the inner leaflet increase rigidity, which presents a substantial barrier to drug penetration.[69] This rigidity correlates with a greater binding energy difference from the global minimum until the nanocluster exits, emphasising the interplay between membrane composition and nanocluster dynamics.

The transport of the small **GEM–CPT** ADDC nanocluster through cancer and normal membranes revealed distinct differences in drug–membrane interactions. In cancer membranes, the binding energy increased steadily as the nanocluster penetrated the membrane, reflecting a stable and efficient transport process (Fig. S4(a)†). In contrast, normal membranes exhibited significant fluctuations in binding energy after reaching the global minimum, indicative of structural disruptions during penetration (Fig. S4(b)†). The cancer membrane remained relatively stable throughout nanocluster transport, resulting in a consistent increase in binding energy with minimal structural changes (Fig. S4(c)†). However, in normal membranes, cholesterol and lipid tails disrupted the nanocluster structure, causing a disordered lipid arrangement that impeded drug release and led to pronounced variations in binding energy (Fig. S4(d)†). These observations underscore the critical role of sterically controlled self-assembly in drug delivery, where disulfide bonds in the **GEM–CPT** nanocluster contribute to membrane disruption, particularly in normal membranes, posing challenges for efficient release and highlighting the need for optimised nanocluster design.

The penetration of both large and small **DOX–HCPT** PND nanoclusters resulted in less membrane disruption due to their π–π stacking structure, which is more sophisticated than the **GEM–CPT** ADDC nanocluster. For the larger nanocluster, the binding energy exhibited significant variations as it traversed

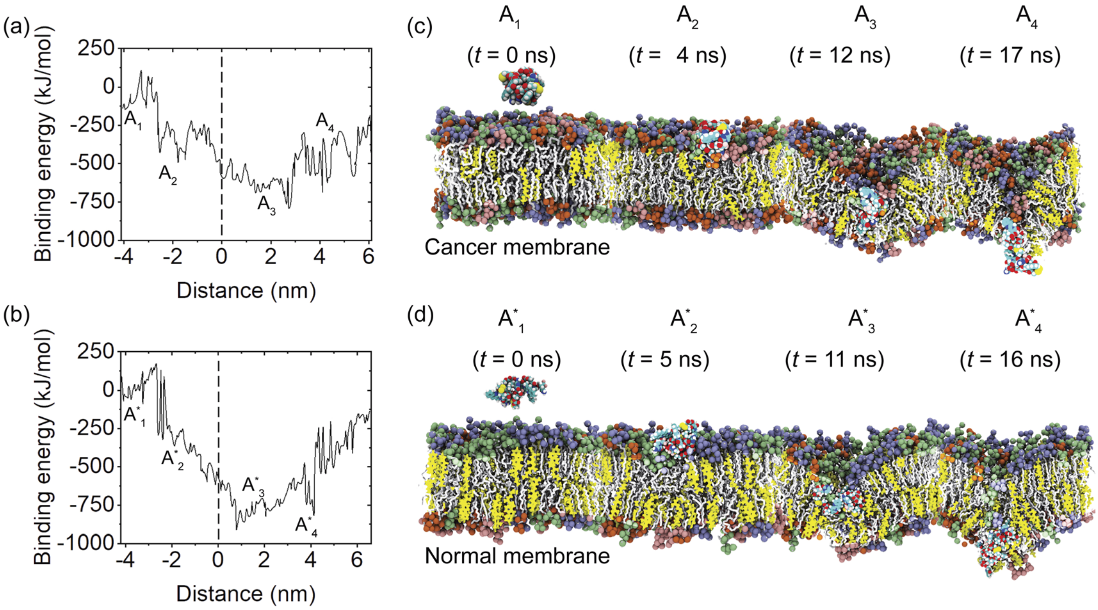

Fig. 5 Binding energies of **GEM–CPT** ADDC nanoclusters interacting with (a) cancer and (b) normal membranes. (c) and (d) present snapshots of the nanoclusters at local energy maxima or minima during their translocation through the cancer and normal membrane models, respectively. Cross-sectional views highlight the nanocluster's position, excluding Na^+, Cl^-, and water molecules for clarity.

the cancer membrane. In contrast, the normal membrane showed notable fluctuations at 4.0 nm beyond the global minimum, as illustrated in Fig. S5(a) and (b).† The minimal disruption occurred in the outer leaflet of the cancer membrane by the drug nanocluster, while the orientation of their π–π stacking resulted in considerable disruption of the inner leaflet of the normal membrane by increasing the contact surface area and binding energy, as demonstrated in Fig. S5(c) and (d).† For the smaller nanocluster, the binding energy decreased significantly in the cancer membrane but increased with fluctuations within a 4 to 6 nm range in the normal membrane, as seen in Fig. S6(a) and (b).† This reduction in the cancer membrane was attributed to van der Waals and electrostatic interactions with the lipid head groups of the inner leaflet, which allowed the membrane to restore its original structure, shown in Fig. S6(c).† In the normal membrane, cholesterol molecules were expelled from the membrane, as shown in Fig. S6(d).† These findings emphasise the role of drug orientation in membrane interaction and disruption, due to the π–π stacking structure of the drug nanocluster, providing information for the development of selective and effective drug delivery systems across various types of membranes.

3.3 Interactions between nanoclusters and lipid bilayer of normal and cancer cells

To gain insights into the interlization mechanisms of the nanoclusters, we examined interactions with lipid head groups (HG) and tail groups (TG). Notable differences in binding energy were observed for large **GEM–CPT** and **DOX–HCPT** nanoclusters that interact with HG and TG in the inner and outer layers of the membrane, as shown in Fig. 6. For HG interactions, the binding energy decreased at approximately −2.9 nm and then increased to a global maximum, which differs from the global minimum observed in the overall membrane model (Fig. 6(a)). The global maximum appeared at roughly 3.2 nm for **GEM–CPT** and around 1.1 nm for **DOX–HCPT**, indicating varying HG disruption due to drug penetration. After global maximum, the binding energy showed pronounced fluctuations until drug release, while both nanoclusters preserved their original structures during penetration (Fig. 6(b) and (c)). In contrast, in TG interactions, the binding energy showed an inverse pattern, slowly declining to a global minimum at approximately 2.0 nm, with minor increases and negligible fluctuations thereafter, as shown in Fig. 6(d). This suggests weaker nanocluster–TG interactions. The **GEM–CPT** nanocluster altered its structure due to the function of the disulfide bond as a foldable joint, while the **DOX–HCPT** nanocluster preserved its structure (Fig. 6(e) and (f)). To provide an atomistic view of the large drug nanoclusters interacting with the cancer membrane, rescaled MD snapshots are available in Fig. S7(a)–(d),† relating to Fig. 6(b), (c), (e) and (f). These results emphasize the unique interaction behaviours of large **GEM–CPT** and **DOX–HCPT** nanoclusters with HG and TG in the cancer membrane, highlighting how structural integrity and lipid perturbation impact binding energy patterns.

Moreover, the interactions between large drug nanoclusters and the HG/TG of a normal membrane displayed distinct variations in the binding energy patterns and drug conformations compared to those of a cancer membrane. Initially, the binding energy decreased around −3.1 nm and increased sharply at ≈3.9 nm, with only minor fluctuations and no steady rise observed between −2.4 and 3.4 nm. This behaviour contrasts with that of the cancer membrane, as shown in Fig. S8(a).† Molecular dynamics snapshots of the **GEM–CPT** and **DOX–**

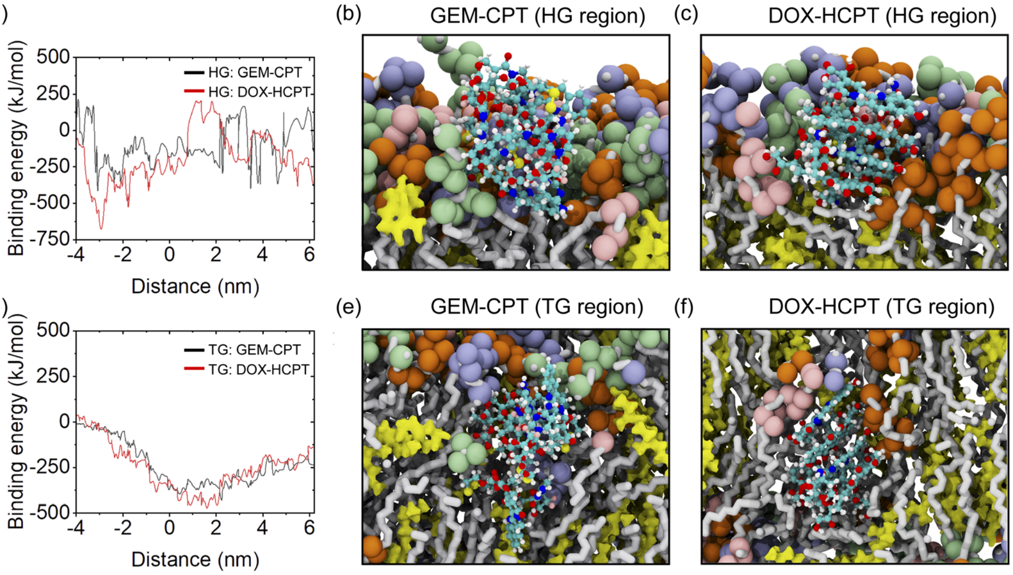

Fig. 6 Binding energies of large **GEM–CPT** (black line) and **DOX–HCPT** (red line) nanoclusters interacting with (a) HG cancer membranes and (d) TG cancer membranes. Snapshots (b and c) show **GEM–CPT** and **DOX–HCPT** nanoclusters at the surface of the HG cancer membrane, while (e and f) depict their positions at the surface of the TG cancer membrane, respectively.

HCPT models that interact with HG are presented in Fig. S8(b) and (c).† In interactions with TG, the binding energy formed a well-shaped curve with variable depths, with the **GEM–CPT** model achieving a more pronounced minimum binding energy than **DOX–HCPT**, indicating a preference for membrane penetration by **GEM–CPT**, as depicted in Fig. S8(d).† However, the **GEM–CPT** nanocluster showed significant structural loss, likely due to its flexible disulfide bond, while the **DOX–HCPT** nanocluster largely preserved its structure, as evidenced in Fig. S8(e) and (f).† These results suggest that the **GEM–CPT** model displays stronger interactions with TG and enhanced structural flexibility, whereas the **DOX–HCPT** model maintains superior structural stability, indicating different interaction mechanics and membrane penetration efficiencies.

For smaller **GEM–CPT** and **DOX–HCPT** nanoclusters, interactions with the HG portion of the cancer cell membrane lead to different trends in binding energy. In contrast, both drug nanoclusters exhibit similar binding energy patterns when interacting with TG. As shown in Fig. S9(a),† the binding energy of **GEM–CPT** decreases at approximately −2.9 nm and increases at around 3.7 nm. Meanwhile, the **DOX–HCPT** nanocluster displays a wave-like pattern caused by electrostatic interactions between its aromatic rings and negatively charged HG lipids (PS and PE). These favourable interactions enable the small **DOX–HCPT** nanocluster to embed into the membrane's outer leaflet. Similar behaviour is seen when the larger **DOX–HCPT** nanocluster crosses the cancer membrane. Interestingly, as shown in Fig. S9 (b) and (c),† **DOX–HCPT** is surrounded by a higher concentration of PS (pink) and PE lipids (orange) compared to **GEM–CPT**. For TG interactions, the binding energy demonstrates a well-shaped profile, with the **GEM–CPT**/TG binding energy having a shallower profile than **DOX–HCPT**, suggesting **DOX–HCPT**'s superior membrane accessibility, as shown in Fig. S9(d).† In particular, as depicted in Fig. S9(e) and (f),† the **DOX–HCPT** nanocluster undergoes more structural alteration, including π–π stacking deformation, while **GEM–CPT** maintains its structural integrity. These observations imply that the strong affinity of **DOX–HCPT** for PS and PE lipids, combined with its structural flexibility, enhances its binding strength and membrane accessibility compared to **GEM–CPT**.

The interactions of small drug nanoclusters with both HG and TG of the normal membrane mirrored those seen with larger nanoclusters, with binding energy decreasing around −3.0 nm and peaking at approximately 3.0 nm, accompanied by significant fluctuations as the drug nanoclusters engaged with HG. Between −2.6 and 2.5 nm, there were minor fluctuations without a steady increase, as illustrated in Fig. S10(a).† The **GEM–CPT** and **DOX–HCPT** drugs interacted with HG by aligning their oxygen-containing groups toward the membrane, as shown in Fig. S10(b) and (c).† Regarding TG interactions, the binding energy showed a well-defined valley for both drug models, although **GEM–CPT** achieved lower energy values beyond 4 nm, as shown in Fig. S10(d),† suggesting similar membrane access for both models. Importantly, both drugs sustained significant structural damage, which is shown in Fig. S10(e) and (f).† These results suggest that despite the fact that both small drug models have comparable TG interaction patterns and membrane access, their structural degradation points to potential stability issues during membrane entry.

The cellular uptake of drugs is significantly influenced by the interactions between drug nanoclusters and HG lipids of cancer cell membranes as well as the structural characteristics of the nanoclusters. Analysis of hydrogen bonds revealed that for larger nanoclusters, the **DOX–HCPT** model formed a higher average number of hydrogen bonds with PE lipids compared to **GEM–CPT**, while no substantial differences were observed with

PS lipids. In particular, the highest number of hydrogen bonds in the **DOX–HCPT** nanocluster occurred at approximately −3 nm, corresponding to the global minimum binding energy, as depicted in Fig. S11.† For smaller nanoclusters, the **DOX–HCPT** model similarly demonstrated hydrogen bonds with PE lipids that were stronger than those with **GEM–CPT**. Furthermore, hydrogen bonds involving PS lipids were observed exclusively in the **DOX–HCPT** model and were absent in the **GEM–CPT** model, as shown in Fig. S12.† These findings highlight that the enhanced π–π stacking structure of **DOX–HCPT** nanoclusters facilitates more efficient drug uptake by cells compared to the steric self-assembly of **GEM–CPT**, emphasising the critical role of structural design in optimising drug delivery systems.

3.4 Impact of co-delivery on membrane deformation

The physicochemical and structural characteristics of a membrane result in significant variations in its deformation and drug-delivery attributes. Initially, the mass density profile of the cancer membrane and the large **GEM–CPT** nanocluster exhibited a balanced distribution of lipids, cholesterol, and water, with no water molecules detected inside the membrane at the beginning of the simulation. By 16 ns, notable shifts in lipid density peaks were observed with the **GEM–CPT** nanocluster, indicating that it disrupts the membrane structure and facilitates lipid rearrangement. In addition, the presence of water molecules within the membrane was observed, as illustrated in Fig. 7(a). MD simulations showed that the hydrophilicity of the **GEM–CPT** nanocluster attracted water molecules, drawing them in as the nanocluster moved through the cancer membrane, as shown in Fig. 7(b). In contrast, the **DOX–HCPT** nanocluster did not cause water infiltration during its penetration, as shown in Fig. 7(c). The hydrophobic nature of **DOX–HCPT** repelled nearby water molecules, discouraging their entry into the membrane and resulting in only slight membrane disturbance, indicated by stable lipid density and relatively shallow insertion, as reflected in Fig. 7(d).

In the examination of large drug models that invade the normal membrane, no water molecules were identified within the membrane, as demonstrated by the MD snapshots in Fig. S13(a) and (b).† Both large nanoclusters caused minimal disturbance to the membrane, the mass density profile indicating a lack of water, and slight alterations in the lipid profiles after drug translocation (occurring at 18 ns for **GEM–CPT** and 17 ns for **DOX–HCPT**), as illustrated in Fig. S13(c) and (d).† Likewise, during the passage of small drug models through the cancer membrane, the hydrophobic core remained devoid of water, as shown in Fig. S14(a) and (b).† However, water was located near the entry points, aligning with membrane restructuring and notable interference. After drug translocation, an asymmetry in the lipid profile was observed, depicted in Fig. S14(c) and (d).† In contrast, the small **GEM–CPT** nanocluster enabled water infiltration into the membrane's interior, while the small **DOX–HCPT** nanocluster resulted in water concentration at the penetration site, as shown in Fig. S15(a) and (b).† These findings were supported by the mass density profile, which revealed water in the centre of the membrane for both small nanoclusters, as shown in Fig. S15(c) and (d).† Consequently, drug attributes such as size, charge, and amphiphilicity are crucial in defining the mechanisms of translocation and membrane permeability related to water infiltration.

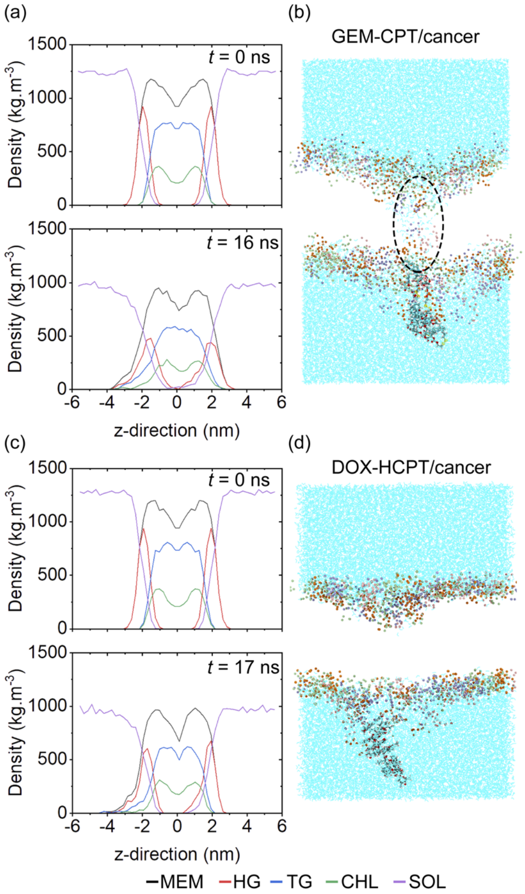

Fig. 7 Mass density profiles of main lipid groups for (a) large GEM–CPT and (c) large DOX–HCPT nanoclusters interacting with the cancer membrane at different simulation times. Snapshots of solvent molecules during the translocation of (b) GEM–CPT and (d) DOX–HCPT nanoclusters across the cancer membrane.

Cholesterol molecules, crucial for maintaining membrane stability, were observed outside the membrane during drug administration. For larger drug models that traverse the cancer cell membrane, CHL molecules remained consistently external to the membrane. However, in normal membranes, the **GEM–CPT** nanocluster effectively extracted cholesterol molecules, a behaviour not observed with the **DOX–HCPT** nanocluster, as shown in Fig. S16.† In the case of smaller drug nanoclusters, cholesterol extraction occurred in both cancerous and normal membranes. This phenomenon is attributed to the high penetration potential of small nanoclusters and structural disturbances induced by TG interactions, which promote cholesterol removal, as shown in Fig. S17.† These findings highlight the structural adaptability of **GEM–CPT** nanoclusters, enabling stronger cholesterol extraction, while **DOX–HCPT** nanoclusters maintain their structural integrity with minimal cholesterol interaction.

4 Conclusions

This study provides a comprehensive molecular understanding of drug penetration through lipid membranes by examining amphiphilic drug–drug conjugates (**GEM–CPT**) and pure nanodrugs (**DOX–HCPT**) using molecular dynamics simulations. **GEM–CPT** demonstrated significant membrane penetration capabilities, effectively disrupting cancer cell membranes by extracting cholesterol and inducing structural alterations, particularly in the inner leaflet, although its flexible disulfide bond led to notable structural instability. In contrast, **DOX–HCPT** maintained structural integrity through stable π–π stacking interactions, allowing selective binding to HG regions and minimal interaction with cholesterol, particularly in normal membranes. Binding energy analysis revealed distinct interaction patterns: **GEM–CPT** exhibited stronger interactions with TG lipids due to its hydrophilic nature, whereas **DOX–HCPT** showed enhanced interactions with HG regions, driven by aromatic stacking and electrostatic complementarity. The size of the nanocluster also played a critical role, with larger clusters exhibiting steric-driven assembly and higher binding fluctuations in cancer membranes, while smaller clusters showed a higher penetration potential but greater structural deformation. Hydration dynamics further distinguished the two systems; **GEM–CPT** attracted water molecules during penetration, enhancing hydrophilic accessibility, while **DOX–HCPT** repelled water due to its hydrophobicity. These findings underscore the distinct interaction mechanisms of hydrophilic **GEM–CPT** and hydrophobic **DOX–HCPT** with lipid membranes, emphasising their respective advantages in disrupting cancerous membranes or maintaining stability in normal membranes. This study offers valuable insights for the design of nanocarriers to improve co-delivery efficiency, target specificity, and therapeutic efficacy.

Data availability

Because of the extensive amount of data associated with the calculation results in this paper, it is not feasible to upload all the data to a public network. However, the relevant calculation data supporting the findings of this study are available within the article and its ESI.† Raw data supporting the findings of this study are available from the corresponding author upon reasonable request.

Conflicts of interest

The authors declare that they have no known competing financial interests or personal relationships that could influence the integrity and objectivity of the findings presented in this article.

Acknowledgements

This work was supported by the Research of Khon Kaen University (RP68-3-002). CC would also like to express our gratitude to the Science Achievement Scholarship of Thailand for financial support.

Notes and references

1 F. Jing, Q. Guo, W. Xu, H. Qu and Z. Sui, *Bioorg. Med. Chem. Lett.*, 2018, **28**, 826–830.
2 V. T. Devita Jr, R. C. Young and G. P. Canellos, *Cancer*, 1975, **35**, 98–110.
3 C. He, Z. Tang, H. Tian and X. Chen, *Adv. Drug Delivery Rev.*, 2016, **98**, 64–76.
4 S.-Y. Qin, A.-Q. Zhang, S.-X. Cheng, L. Rong and X.-Z. Zhang, *Biomater. Sci*, 2017, **112**, 234–247.
5 Q. Song, X. Wang, Y. Wang, Y. Liang, Y. Zhou, X. Song, B. He, H. Zhang, W. Dai, X. Wang, *et al.*, *Mol. Pharmaceutics*, 2016, **13**, 190–201.
6 C. Gao, P. Bhattarai, M. Chen, N. Zhang, S. Hameed, X. Yue and Z. Dai, *Bioconjugate Chem.*, 2018, **29**, 3967–3981.
7 P. Huang, D. Wang, Y. Su, W. Huang, Y. Zhou, D. Cui, X. Zhu and D. Yan, *J. Am. Chem. Soc.*, 2014, **136**, 11748–11756.
8 M. Sun, Q. Qian, L. Shi, L. Xu, Q. Liu, L. Zhou, X. Zhu, J.-M. Yue and D. Yan, *Sci. China:Chem.*, 2020, **63**, 35–41.
9 M. Hou, P. Xue, Y.-E. Gao, X. Ma, S. Bai, Y. Kang and Z. Xu, *Biomater. Sci.*, 2017, **5**, 1889–1897.
10 S. Fu, G. Li, W. Zang, X. Zhou, K. Shi and Y. Zhai, *Acta Pharm. Sin. B*, 2022, **12**, 92–106.
11 M. N. Holme, I. A. Fedotenko, D. Abegg, J. Althaus, L. Babel, F. Favarger, R. Reiter, R. Tanasescu, P.-L. Zaffalon, A. Ziegler, *et al.*, *Nat. Nanotechnol.*, 2012, **7**, 536–543.
12 C.-M. J. Hu and L. Zhang, *Biochem. Pharmacol.*, 2012, **83**, 1104–1111.
13 L. Feng, M. Gao, D. Tao, Q. Chen, H. Wang, Z. Dong, M. Chen and Z. Liu, *Adv. Funct. Mater.*, 2016, **26**, 2207–2217.
14 Q. Liu, J. Zhang, W. Sun, Q. R. Xie, W. Xia and H. Gu, *Int. J. Nanomed.*, 2012, 999–1013.
15 S. Shirazi-Fard, A. R. Zolghadr and A. Klein, *New J. Chem.*, 2023, **47**, 22063–22077.
16 M. Ibrahim, W. H. Abuwatfa, N. S. Awad, R. Sabouni and G. A. Husseini, *Pharm.*, 2022, **14**, 254.
17 F. Chen, Y. Zhao, Y. Pan, X. Xue, X. Zhang, A. Kumar and X.-J. Liang, *Mol. Pharm.*, 2015, **12**, 2237–2244.
18 R. Zhang, X. Qin, F. Kong, P. Chen and G. Pan, *Drug Delivery*, 2019, **26**, 328–342.
19 A. Preetha, R. Banerjee, N. Huilgol, *et al.*, *J. Cancer Res. Ther.*, 2005, **1**, 180–186.
20 P. P. Hsu and D. M. Sabatini, *Cell*, 2008, **134**, 703–707.
21 C. R. Santos and A. Schulze, *FEBS J.*, 2012, **279**, 2610–2623.
22 J. V. Swinnen, F. Vanderhoydonc, A. A. Elgamal, M. Eelen, I. Vercaeren, S. Joniau, H. Van Poppel, L. Baert, K. Goossens, W. Heyns, *et al.*, *Int. J. Cancer*, 2000, **88**, 176–179.
23 F. P. Kuhajda, *Cancer Res.*, 2006, **66**, 5977–5980.
24 N. Azordegan, V. Fraser, K. Le, L. M. Hillyer, D. W. Ma, G. Fischer and M. H. Moghadasian, *Mol. Cell. Biochem.*, 2013, **374**, 223–232.

25 T. E. Merchant, J. N. Kasimos, T. Vroom, E. de Bree, J. L. Iwata, P. W. de Graaf and T. Glonek, *Cancer Lett.*, 2002, **176**, 159–167.

26 P. V. Escriba, A. V. Ferrer-Montiel, J. A. Ferragut and J. M. Gonzalez-Ros, *Biochem.*, 1990, **29**, 7275–7282.

27 G. van Meer, *Cold Spring Harbor Perspect. Biol.*, 2011, **3**, a004671.

28 G. Van Meer, D. R. Voelker and G. W. Feigenson, *Nat. Rev. Mol. Cell Biol.*, 2008, **9**, 112–124.

29 T. Rivel, C. Ramseyer and S. Yesylevskyy, *Sci. Rep.*, 2019, **9**, 1–14.

30 R. Hirano, T. Kagamiya, Y. Matsumoto, T. Furuta and M. Sakurai, *Biochem. Biophys. Rep.*, 2021, **25**, 100913.

31 E. Lindahl, M. Abraham, B. Hess and D. Van der Spoel, *GROMACS Development Team*: Stockholm, Sweden, 2020.

32 D. A. Case, T. E. Cheatham III, T. Darden, H. Gohlke, R. Luo, K. M. Merz Jr., A. Onufriev, C. Simmerling, B. Wang and R. J. Woods, *J. Comput. Chem.*, 2005, **26**, 1668–1688.

33 R. Salomon-Ferrer, D. A. Case and R. C. Walker, *Wiley Interdiscip. Rev.: Comput. Mol. Sci.*, 2013, **3**, 198–210.

34 W. Phanchai, J. Thonghlueng and T. Puangmali, *ACS Appl. Nano Mater.*, 2024, **7**, 5554–5563.

35 P. Toomjeen, W. Phanchai, C. Choodet, A. Chompoosor, R. Thanan, C. Sakonsinsiri and T. Puangmali, *J. Phys. Chem. B*, 2019, **123**, 1129–1138.

36 K. L. Rhinehardt, G. Srinivas and R. V. Mohan, *J. Phys. Chem. B*, 2015, **119**, 6571–6583.

37 M. Rezaeisadat, A.-K. Bordbar and R. Omidyan, *J. Mol. Liq.*, 2021, **332**, 115862.

38 P. Stipa, S. Marano, R. Galeazzi, C. Minnelli, G. Mobbili and E. Laudadio, *Eur. Polym. J.*, 2021, **147**, 110292.

39 A. Kabedev, S. Hossain, M. Hubert, P. Larsson and C. A. Bergström, *J. Pharm. Sci.*, 2021, **110**, 176–185.

40 U. Srikulwong, W. Phanchai, P. Srepusharawoot, C. Sakonsinsiri and T. Puangmali, *J. Phys. Chem. B*, 2021, **125**, 6697–6708.

41 W. Phanchai, U. Srikulwong, A. Chuaephon, S. Koowattanasuchat, J. Assawakhajornsak, R. Thanan, C. Sakonsinsiri and T. Puangmali, *ACS Appl. Nano Mater.*, 2022, **5**, 9042–9052.

42 W. L. Jorgensen, J. Chandrasekhar, J. D. Madura, R. W. Impey and M. L. Klein, *J. Chem. Phys.*, 1983, **79**, 926–935.

43 W. Humphrey, A. Dalke and K. Schulten, *J. Mol. Graphics*, 1996, **14**, 33–38.

44 J. Wang, W. Wang, P. A. Kollman and D. A. Case, *J. Am. Chem. Soc.*, 2001, **222**, 2001.

45 S. Jo, T. Kim, V. G. Iyer and W. Im, *J. Comput. Chem.*, 2008, **29**, 1859–1865.

46 J. Lee, D. S. Patel, J. Ståhle, S.-J. Park, N. R. Kern, S. Kim, J. Lee, X. Cheng, M. A. Valvano, O. Holst, et al., *J. Chem. Theory Comput.*, 2018, **15**, 775–786.

47 A.-R. Allouche, *J. Comput. Chem.*, 2011, **32**, 174–182.

48 D. L. Daleke, *Curr. Opin. Hematol.*, 2008, **15**, 191–195.

49 A. C. Alves and D. Ribeiro and Nunes, *Biochim. Biophys. Acta, Biomembr.*, 2016, **1858**, 2231–2244.

50 T. J. Desai, J. E. Toombs, J. D. Minna, R. A. Brekken and D. G. Udugamasooriya, *Oncotarget*, 2016, **7**, 30678.

51 B. Park, *Biophys. J.*, 2024, **123**, 372a.

52 F. Włodek, W. Kulig and A. Stachowicz-Kuśnierz, *Biochim. Biophys. Acta*, 2024, **1866**, 184327.

53 C. A. Lochbaum, A. K. Chew, X. Zhang, V. Rotello, R. C. Van Lehn and J. A. Pedersen, *ACS Nano*, 2021, **15**, 6562–6572.

54 T. Lunnoo, J. Assawakhajornsak and T. Puangmali, *J. Phys. Chem. C*, 2019, **123**, 3801–3810.

55 P. A. Kollman, I. Massova, C. Reyes, B. Kuhn, S. Huo, L. Chong, M. Lee, T. Lee, Y. Duan, W. Wang, *et al.*, *Acc. Chem. Res.*, 2000, **33**, 889–897.

56 D. Greene, R. Qi, R. Nguyen, T. Qiu and R. Luo, *J. Chem. Inf. Model.*, 2019, **59**, 3041–3056.

57 R. Kumari, R. Kumar, O. S. D. D. Consortium and A. Lynn, *J. Chem. Inf. Model.*, 2014, **54**, 1951–1962.

58 K. Sztandera, M. Gorzkiewicz, E. A. Zizzi, N. Dybczak, L. Poltorak, M. A. Deriu and B. Klajnert-Maculewicz, *Bioelectrochemistry*, 2023, **152**, 108449.

59 A. Kumar, B. Mishra, A. D. Konar, E. Mylonakis and A. Basu, *J. Phys. Chem. B*, 2024, **128**, 6049–6058.

60 Z. Cao, L. Liu, G. Hu, Y. Bian, H. Li, J. Wang and Y. Zhou, *Biochim. Biophys. Acta*, 2020, **1862**, 183402.

61 E. Wang, H. Sun, J. Wang, Z. Wang, H. Liu, J. Z. Zhang and T. Hou, *Chem. Rev.*, 2019, **119**, 9478–9508.

62 N. Homeyer and H. Gohlke, *Mol. Inf.*, 2012, **31**, 114–122.

63 Y. Xu, Y. Huang, X. Zhang, W. Lu, J. Yu and S. Liu, *Int. J. Pharm.*, 2018, **550**, 45–56.

64 R. Menichetti, K. H. Kanekal and T. Bereau, *ACS Cent. Sci.*, 2019, **5**, 290–298.

65 P. K. Tang, K. Chakraborty, W. Hu, M. Kang and S. M. Loverde, *J. Chem. Theory Comput.*, 2020, **16**, 3373–3384.

66 C. H. Tse, J. Comer, Y. Wang and C. Chipot, *J. Chem. Theory Comput.*, 2018, **14**, 2895–2909.

67 P. Siani, E. Donadoni, L. Ferraro, F. Re and C. Di Valentin, *Biochim. Biophys. Acta*, 2022, **1864**, 183763.

68 Y. Zhao, Y. Zhao, Q. Ma, B. Sun, Q. Wang, Z. Ding, H. Zhang, X. Chu, M. Liu, Z. Wang, *et al.*, *Int. J. Nanomed.*, 2019, 8665–8683.

69 R. Dawaliby, C. Trubbia, C. Delporte, C. Noyon, J.-M. Ruysschaert, P. Van Antwerpen and C. Govaerts, *J. Biol. Chem.*, 2016, **291**, 3658–3667.